Scientia Iranica D (2023) 30(3), 1106–1126

Sharif University of Technology
Scientia Iranica
Transactions D: Computer Science & Engineering and Electrical Engineering
http://scientiairanica.sharif.edu

Mathematical modeling of PMSG-based wind power plants for harmonic resonance studies and analytical assessment of wind turbine converters' controls on the harmonic resonance response of the plants

A. Beiki and M. Rahimi*

Department of Electrical and Computer Engineering, University of Kashan, Kashan, P.O. Box 87317-53153, Iran.

Received 1 January 2021; received in revised form 27 June 2021; accepted 1 November 2021

KEYWORDS
Wind power plant;
Harmonic resonance;
Harmonic impedance model;
Frequency scan;
Harmonic resonance mode analysis.

Abstract. In this paper, harmonic resonance analysis of the grid comprising Wind Power Plants (WPPs) with Permanent Magnet Synchronous Generators (PMSGs) is presented. Usually, Norton equivalent circuit is used as the Wind Turbine (WT) model for harmonic resonance studies, in which the WTs are simply modeled as ideal current and voltage sources and the impacts of converters controls on the WTs output impedances are neglected. This paper deals with the harmonic resonance analysis of the WPP system by considering the impacts of converters controls and current and voltage measurement filters. In doing so, harmonic impedance models of the WTs are presented for simple and detailed cases. Then, the WT harmonic impedance is extracted for the mentioned cases. Next, the results of frequency scan and harmonic mode resonance analyses for different cases are given and compared. Then, the effects of the current and voltage measurement filters and WT converter control on harmonic resonance analysis of the study WPP system are presented. It is shown that increasing the bandwidth of the grid-side converter current control loop cannot shift the resonant frequencies, but it certainly enhances the system damping and, consequently, reduces the driving point impedances in the resonant frequencies.

1. Introduction

Variable Speed Wind Turbines (VSWTs) employing Voltage Source Converters (VSCs) are widely used in wind energy conversion systems. VSWTs are mainly divided into two main groups: VSWTs with fractional converters known as Doubly Fed Induction Generator (DFIG) based WTs, and VSWTs with fully rated converters employing Permanent Magnet Synchronous Generators (PMSGs), electrical excited synchronous generators, and Squirrel Cage Induction Generators (SCIGs). Recently, due to their simple structure, enhanced power factor, and efficient energy conversion, VSWTs with PMSGs are used in Wind Power Plants (WPPs) [1–6].

A large number of power electronic converters are used in VSWT-based WPPs which are the main reason of harmonics emission. In the PMSG-based WPPs, the switching operation of back-to-back VSCs is the main reason for the propagation of harmonics.

These harmonics may be magnified due to oc-

---

*. *Corresponding author.*
E-mail address: mrahimi@kashanu.ac.ir (M. Rahimi)

doi: 10.24200/sci.2021.57372.5204

currence of resonance in the grid close to the harmonic frequencies [7–10]. The subject of harmonic and resonance problems in the grid with WPPs was studied in [11–13]. In general, there are two types of resonances known as parallel and series resonances [14]. In the literature, parallel resonance studies are usually presented in the grid integrated WPPs [7–13].

Traditionally, there are two resonance identification techniques: the first one is Frequency Scan (FS) analysis that is used to identify the resonance frequencies, while the second one is Harmonic Resonance Mode Analysis (HRMA) approach that is used to calculate the harmonic resonance modes related to different network buses [15–19]. These two methods together provide a comprehensive understanding of the resonance frequencies and their centers in the network. With the recognition of resonant frequencies in WPPs, it is possible to filter harmonics with frequencies close to the resonance frequency and prevent the occurrence of resonance phenomenon [20,21].

There are several papers on the harmonic resonance studies in the power networks comprising WPPs [22–38]. In [22], authors demonstrated that WPP components such as widespread medium-voltage cable system and offshore grid transformers could introduce significant low-frequency parallel resonances that could cause a significant harmonic voltage distortion at the point of common coupling. In [23], a study on harmonic resonances in an offshore WPP was presented, and the sensitivity analysis was employed to decide the best location of the filters for compensating the harmonics in a WPP. In [24], possible instability of the AC bus voltage and resonance between the wind farm and the HVDC rectifier were examined through the analysis of the system impedance model. In [25], an extended harmonic domain model of DFIG WT including both electrical and mechanical subsystems was presented to monitor step-by-step harmonics time variation and to detect contingency scenarios such as resonance problems caused by a specific harmonic.

In recent studies, impedance-based modeling has been used as the Wind Turbine (WT) model for the harmonic resonance studies [26–30]. In some research works, WTs are simply modeled as ideal current and voltage sources for harmonic resonance studies and the impacts of the WT control on the impedance modeling of WPP are neglected [31–33]. However, these simple WTs models may result in inaccurate results, because the impact of the WT control on harmonic resonance studies is neglected [34,35].

There are also a few publications regarding the harmonic resonance studies taking the wind turbine converter control into account [36–38]. In [36], the effect of WT converter control on WPP harmonic response was investigated, and some expressions were presented for WT equivalent harmonic impedance including current control of the WT converter. Researchers in [37] presented a method for the WT inner controllers in the case of a PMSG-based wind farm in order to reduce the number of resonances and mitigate harmonic instability. The study in [38] investigated the resonance issues caused by the submarine transmission cable in a grid-connected offshore wind farm and proposed a cascaded notch-filter-based active damping method to guarantee good system stability and robustness.

It is noted that not only the WTs controls affect harmonic resonance studies, but also the cut-off frequencies of the current and voltage measurements affect the results of harmonic resonance analysis. Besides, there are few comparisons between the simple and detailed WTs models for harmonic resonance studies. The issue that gains significance in harmonic resonance studies is that the result of which simple model 'in what frequency range' and 'for which values of the controller bandwidth' could fit the results of detailed WT model. Hence, in related publications, few analytical works have been published regarding the full modeling of WTs for harmonic resonance studies by considering the effects of WT converter controllers and current and voltage measurement filters.

The main outlines of this study are given as follows. This paper deals with the harmonic resonance analysis of the study WPP system by considering the impacts of the WT Grid-Side Converter (GSC) control as well as current and voltage measurement filters. The system under study in this paper is a 400 MW WPP comprising PMSG-based WTs connected to a 150 kV grid through interfaced LCL filters, cables, and power transformers. In doing so, the WT harmonic impedance models of the WTs are presented for three simple cases (cases A, B, and C) and one detailed case (Case D). Then, the WT harmonic output impedance is calculated for the mentioned cases. In the mentioned simple cases, the dynamics of the current and voltage measurement filters and WT current controller are neglected and simple expressions are extracted for the WT equivalent harmonic impedance.

Next, the FS and HRMA results related to different simple and detailed cases are given and compared. Then, the effects of the bandwidths of the current and voltage measurements filters and impact of the closed-loop bandwidth of the WT current control loop on harmonic resonance analyses of the study WPP system are studied and investigated.

It is shown that at a sufficiently large value of current measurement filter bandwidth and a small value of voltage measurement filter bandwidth, the model of Case D can be approximated by the model of Case B. In addition, it is depicted that increasing the bandwidth of the current control loop cannot shift the resonant frequencies, but it enhances the system damping and, consequently, reduces the driving point impedances in the resonant frequencies.

2. Resonance phenomenon

Resonance phenomenon is defined as the exchange of energy between capacitive and inductive components in an electric network. Therefore, at least, one capacitive and one inductive element should be present in a network for resonance interaction to occur. In an LC circuit, the capacitive and inductive components of the network begin to resonate with each other at a frequency called the resonance frequency ($f_{res} = \frac{1}{2\pi\sqrt{LC}}$) [39]. Under a condition in which the resonance frequency coincides with a frequency of any harmonic current or voltage, the harmonic current and voltage can be amplified, which may damage the network elements. In an electric network, depending on the network configuration, there might be multiple resonance frequencies [40]. Two types of resonances may occur in electrical circuits: parallel resonance and series resonance.

The parallel resonance can be demonstrated by the circuit of Figure 1, in which the equivalent circuit reactance is $X_{eq} = \frac{L\omega}{1-\omega^2 LC}$. At the resonance frequency, the denominator of equivalent reactance is equal to zero and thus, the equivalent reactance is infinite and all harmonic currents are directed to the resistance of the circuit. A parallel resonance depicts a high impedance at the harmonic current close to the resonance frequency. In this case, a small harmonic current close to the resonance frequency may result in high voltage distortion.

A simple-series RLC circuit that describes the series resonance is shown in Figure 2, in which the equivalent circuit reactance is $X_{eq} = \frac{\omega^2 LC-1}{\omega C}$. At the resonance frequency, the equivalent reactance becomes equal to zero and the current path impedance decreases; thus, even a relatively small harmonic voltage can generate a large current around the resonance frequency [41].

3. Resonance identification techniques

This section introduces the main features of two mathematical approaches used for identifying resonances in electrical grid. These methods are known as FS and HRMA. Both of these approaches are used in the next sections for the analytical study of harmonic resonance in grid-connected wind farms.

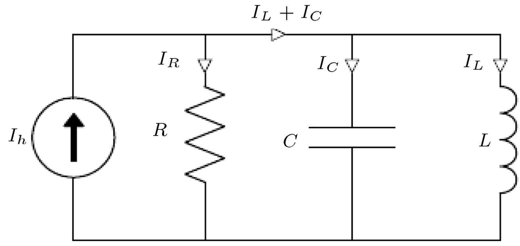

Figure 1. Parallel RLC circuit.

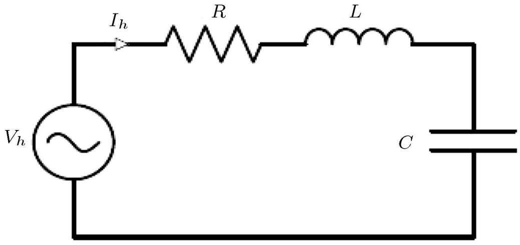

Figure 2. Series RLC circuit.

3.1. *Frequency Scan (FS)*

The main objective of the FS method is to find possible resonance frequencies in an electric network [18]. A k-bus electric network can be represented by a $k \times k$ admittance matrix, Y_{bus}. The relationship between buses voltages and currents at any harmonic frequency can be given as $[I_h] = [Y_h][V_h]$.

In the FS method, a per unit current with frequency of f_h is injected into a certain bus and the corresponding voltage is calculated by the following equation:

$$[V_h] = [Y_h]^{-1}[I_h] = [Z_h][I_h], \quad (1)$$

where h is the harmonic order, $[V_h]$ is the vector of nodal harmonic voltages, $[Y_h]$ is the harmonic admittance matrix, $[Z_h]$ is the harmonic impedance matrix, and $[I_h]$ is the vector of injected harmonic currents [42]. The diagonal elements of the impedance matrix are known as the driving point impedances. The results of FS method are plots of the magnitudes of the driving point impedances at different harmonic frequencies.

As noted in Section 2, the impedance magnitude increases considerably in parallel resonance and decreases sharply in series resonance. Therefore, the peak of the FS diagram represents parallel resonance and the dip one denotes the series resonance [43]. Although FS method is very convenient and simple, it is not possible to identify the system parameters and variables involved in resonance modes. To overcome this limitation, the method described in Section 3.2 is also used for accurate resonance analysis of the study electrical network.

3.2. *Harmonic Resonance Mode Analysis (HRMA)*

HRMA is used for parallel resonance identification in an electric network. In the HRMA method, instead of the nodal voltage and current vectors and nodal impedance, the concepts of the modal voltage and current vectors and modal impedance are given. Based on the HRMA approach, at resonance frequencies, the network admittance matrix $[Y_h]$ becomes singular and, at least, one of the eigenvalues of the $[Y_h]$ matrix reaches zero value. At the parallel resonance frequencies, some nodal voltages may get larger and thus, the determinant of the $[Y_h]$ matrix becomes very small.

The admittance matrix can be given in the form of the following equation as the product of three matrices:

$$[Y_h] = [\psi_h] [\Lambda_h] [\Phi_h] , \tag{2}$$

where $[\psi_h]$ and $[\Phi_h]$ are the left and right eigenvector matrices, respectively. Also, $[\Lambda_h] = diag(\lambda_1, \lambda_2, ..., \lambda_n)$ is the diagonal eigenvalue matrix related to admittance matrix $[Y_h]$. The left eigenvector matrix is the inverse of the right eigenvector matrix as $[\Phi_h] = [\Psi_h]^{-1}$. From Eqs. (1) and (2), the relation between the harmonic nodal voltages and currents is obtained as follows:

$$[V_h] = [\Psi_h] [\Lambda_h]^{-1} [\Phi_h] [I_h] . \tag{3}$$

Eq. (3) can be given in the following form:

$$[V_m] = [\Lambda_h]^{-1} [I_m] = [Z_m] [I_m] , \tag{4}$$

where $[V_m]$ ($[V_m] = [\Phi_h] [V_h]$) is the modal voltage vector, $[I_m]$ ($[I_m] = [\Phi_h] [I_h]$) is the modal current vector, and $[Z_m] = [\Lambda_h]^{-1}$ is called modal impedance matrix [44]. The mode with the eigenvalue closer to zero corresponds to a high modal impedance and is known as the critical mode; thus, the frequency corresponding to this mode is called the resonance frequency. The plot of the modal impedance as a function of the frequency is known as the modal impedance plot [45].

The value of the impedance seen from the bus j, i.e., driving point impedance of bus j, is calculated through the following equation:

$$Z_{jj} = PF_{j1} \times Z_{m1} + PF_{j2} \times Z_{m2}$$
$$+ ... + PF_{jn} Z_{mn}, \tag{5}$$

where PF_{ji} is the participation factor of bus j in the ith mode, Z_{mi} is the modal impedance associated to the ith eigenvalue λ_i, and n refers to the number of the modes. In other words, participation factor indicates how much each mode is involved in the impedance seen from each bus. The participation factor of bus j in the ith mode PF_{ki} can be given as $PF_{ji} = \psi_{ij}\phi_{ji}$, where ψ_{ij} and ϕ_{ji} are the jth elements of the ith left and right eigenvectors. The total participation factor of all buses in each mode is equal to one.

4. System under study description

In this section, the system under study comprising an aggregated model of a 400 MW WPP is described and then, a simplified model of the system is introduced for resonance analysis.

Figure 3 shows the aggregated model of the 400 MW-WPP with a radial topology consisting of four branches. Each branch is formed by fifty 2 MW full converter PMSG-WTs with a terminal voltage of 690 V. In this aggregated model, the fifty WTs in each branch are modeled as a single WT representing a 100 MW WT. Each aggregated WT includes a PMSG, back-to-back VSCs, LCL filter, and a 690 V/33 kV transformer. All transmission cables are considered as π-model. In Figure 3, both branches 2 and 4 are connected to branches 1 and 3 through 33 kV cables with lengths of 8 km. All four groups are connected to the 150 kV grid via two 33 kV/150 kV transformers and two 33 kV transmission cables with a length of 8 km. On the 150 kV side, a 150 kV transmission line with length of 58 km together with a power transformer transmits the WPP power to the grid. In the Appendix, all parameters of the study

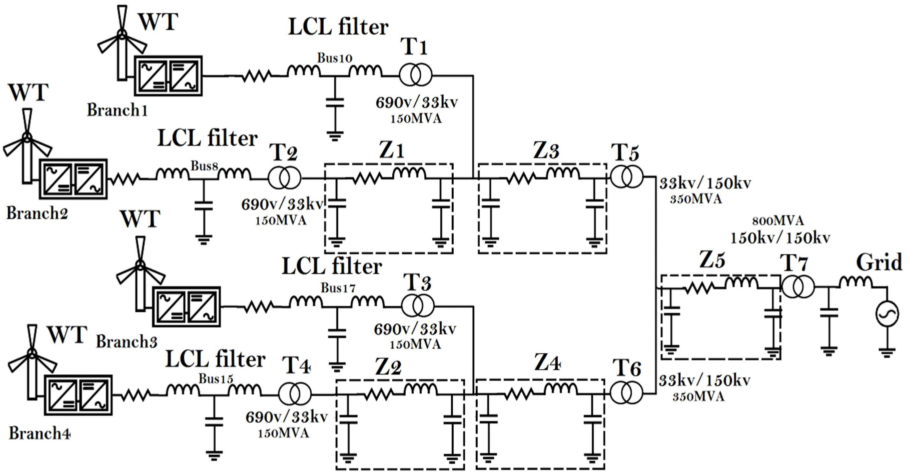

Figure 3. Single line diagram of the study 400 MW-WPP connected to the grid.

system of Figure 3 are given, where for simplicity all parameters are referred to the 150 kV side of the network.

The switching process of the converters generates harmonics in the output current of the converters. As a result, the LCL filter related to each WT limits these harmonics. The resonance frequency of the LCL filters (f_{res}) should be selected such that $10f_1 \leq f_{res} \leq 0.5f_{sw}$, where f_1 ($f_1 = 50$ Hz) is the fundamental frequency and f_{sw} ($f_{sw} = 2$ kHz) is the back-to-back converters switching frequency. The resonance frequency of the LCL filter can be obtained as $f_{res} = \frac{1}{2\pi}\sqrt{\frac{L_{f1}+L_{f2}}{L_{f1}L_{f2}C}}$ in (Hz), where L_{f1} and L_{f2} are converter and grid side inductances, respectively.

5. Harmonic impedance modeling of WPP considering WT control impact

Figure 4 shows a grid-connected PMSG-WT in which GSC is connected to the grid via LCL filter and step-up transformer.

The GSC is controlled in the synchronous reference frame with grid voltage orientation, in which $v_{gd} = V_g$ and $v_{gq} = 0$. One of the important issues in the WPP resonance analysis is the WT modeling, where the Norton equivalent circuit of the WT is employed in this paper. Figure 5 shows the Norton equivalent circuit of the WT system of Figure 4 in which from the grid voltage (V_g) point of view, the WT system is modeled as a current source in parallel with the output impedance $Z_{o,WT}(s)$. According to Figure 5, the WT system consists of PMSG, MSC, GSC, inductance filter L_{f1}, and converter controllers.

In Figure 3, buses 8, 10, 15, and 17 are the points to which aggregated WT systems are connected. By replacing each aggregated WT system in Figure 3 with the corresponding Norton equivalent model, the Norton equivalent model of the study system is obtained, as depicted in Figure 6.

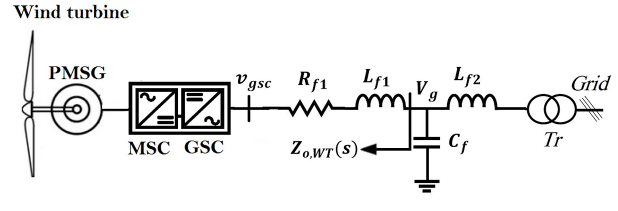

Figure 4. Grid-connected PMSG-WT.

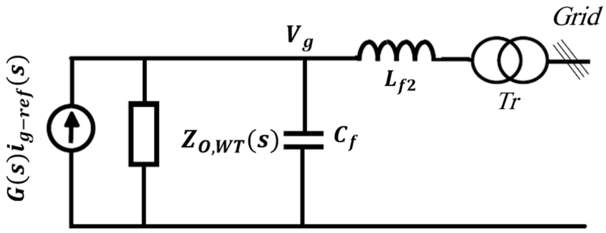

Figure 5. Norton equivalent circuit of the WT system.

The output impedance $Z_{o,WT}(s)$ in Figure 7 is dependent on the GSC control system. Figure 7 shows the overall control structure of the GSC control in the *dq* reference frame [46]. Also, Figure 8 shows the GSC inner current control loop.

It is noted that the GSC in this paper is controlled in the *dq* rotating reference frame. The GSC control architecture in this paper is based on double-loop control structure comprising outer and inner control loops. Since the GSC is modeled and controlled in the *dq* rotating reference frame, PI controllers are used in the outer and inner control loops. The main tasks of the GSC are keeping the dc-link voltage constant and exchanging reactive power with the grid. Hence, the reference currents *igd-ref* and *igq-ref* in Figures 7 and 8 are obtained from the outer dc-link and reactive power control loops.

Since the dynamics of the outer dc-link and reactive power control loops are slow, the effects of outer control loops on the WPP harmonic resonance modeling are neglected. Hence, $Z_{o,WT}(s)$ is affected by the dynamics of the inner current control loops. $T_i(s)$ and $T_v(s)$ in Figure 8 represent the dynamics of the grid voltage and current measurements and signal filtering and are described by the first-order transfer functions $T_i(s) = 1/(1 + s\tau_i)$ and $T_v(s) = 1/(1 + s\tau_v)$ with time constants of τ_i and τ_v.

If the closed-loop bandwidth of the GSC control loop ω_i is sufficiently small against $1/\tau_i$, i.e., $\omega_i << 1/\tau_i$, we can neglect the dynamics of $T_i(s)$ for the current controller design. Hence, assuming $PI(s) = k_p + k_i/s$ and using the pole-zero cancellation approach, k_p and k_i are obtained as $k_p = L_{f1}\omega_i$ and $k_i = R_{f1}\omega_i$, where ω_i is the current control closed-loop bandwidth.

Also, $\hat{i}_{gdq}$ and $\hat{v}_{gdq}$ in Figure 8 are associated with the filtered converter current and grid voltage.

5.1. WT equivalent output impedance considering the GSC control

From Figures 4 and 8, the dynamics of the GSC in the rotating dq frame and in the s-domain can be given as:

$$v_{gsc}(s) = (R_{f1} + jL_{f1}\omega_0 + L_{f1}s)\, i_g(s) + v_g(s), \quad (6)$$

where ω_0 is the grid fundamental frequency. Also, from Figure 8, v_{gsc} can be given as:

$$v_{gsc}(s) = PI(s)\,(i_{g-ref}(s) - T_i(s)i_g(s)) \\ +T_v(s)v_g(s) + jL_{f1}\omega_0 T_i(s)i_g(s). \quad (7)$$

From Eqs. (6) and (7) and by setting $i_{g-ref} = 0$, the WT output impedance in the *dq* reference frame is obtained as:

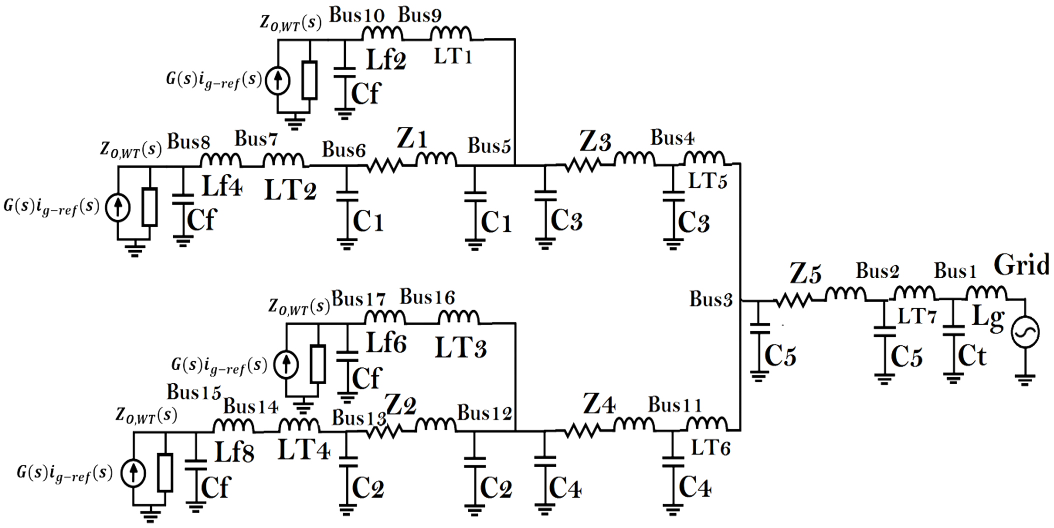

Figure 6. Norton equivalent circuit of the system under study.

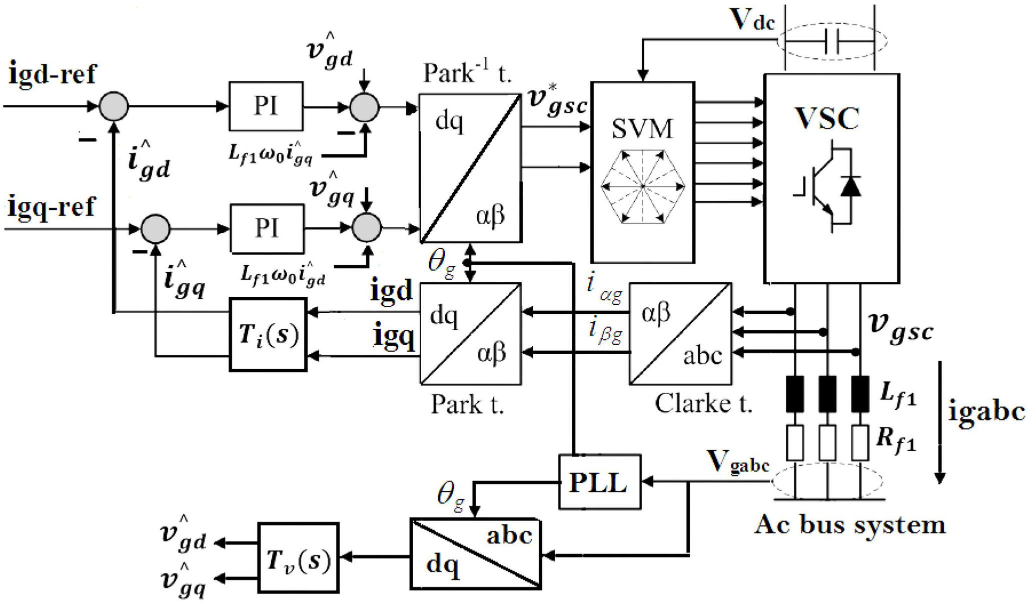

Figure 7. Overall control structure of the GSC.

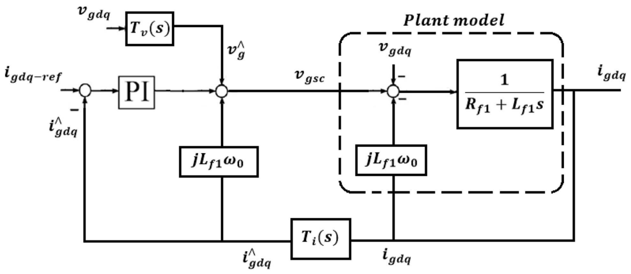

Figure 8. GSC inner current control loop.

$$Z_{odq,WT}(s)=\frac{v_g(s)}{-i_g(s)}=$$

$$\frac{R_{f1}+L_{f1}s+PI(s)T_i(s)+jL_{f1}\omega_0(1-T_i(s))}{1-T_v(s)}. \tag{8}$$

According to Eq. (8), $Z_{odq,WT}(s)$ depends on LCL filter parameters (i.e., L_{f1} and R_{f1}), GSC PI controller parameters (k_p and k_i), and current/voltage measurements dynamics ($T_i(s)$ and $T_v(s)$).

The WT output impedance in Figure 5 is the equivalent impedance of the WT in the *abc* stationary frame. The equivalent output impedance of the WT at the kth harmonic is obtained by substituting s with $jk\omega_0$ at $Z_{oWT}(s)$ where ω_0 is the fundamental frequency.

The control structure of the GSC in Figure 8 is in the dq synchronous reference frame. In a dq reference frame rotating at the synchronous frequency of ω_0, the positive sequence of the kth harmonic appears as a harmonic with frequency of $(k-1)\omega_0$. Also, the

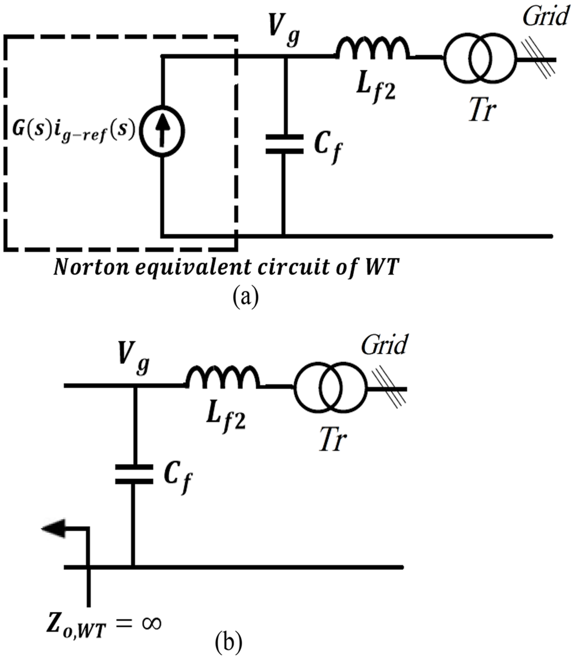

Figure 9. (a) Norton equivalent circuit of the WT system in Case A, (b) Equivalent harmonic impedance of the WT system in Case A.

negative sequence of the kth harmonic appears as a harmonic with frequency of $-(k+1)\omega_0$ in the dq frame.

Considering the above explanations, relation between $Z_{o,WT}(s)$ and $Z_{odq,WT}(s)$ for the kth harmonic is obtained as given in Eq. (9) in Box I. It is noted that in Eq. (9), $Z_{o,WT}$ is the WT output impedance in the abc frame and $Z_{odq,WT}$ is the WT output impedance at in rotating dq reference frame.

In the following, four different cases are considered and for each case, the WT equivalent harmonic impedance is extracted and in Sections 6 and 7, HRMA and FS results are presented.

Case A: In this case, the grid voltage is feed forwardly compensated, and the bandwidths of the current and voltage filters ($T_i(s)$ and $T_v(s)$) are considered sufficiently large, i.e., $T_i(s) = 1$ and $T_v(s) = 1$. In this case, from Eqs. (8) and (9), $Z_{o,WT}(s)$ is obtained as $Z_{o,WT}(s) = \infty$. Thus, in the Norton equivalent circuit, each WT is modeled as a current source. Figure 9(a) and (b) show the Norton equivalent circuit and equivalent harmonic impedance of the WT system of Figure 4. According to Figure 9, in this case, the WT control does not add a positive damping action.

Case B: In this case, the grid voltage is not feed forwardly compensated, i.e., $T_v(s) = 0$, and the bandwidth of the current measurement filter $T_i(s)$ is considered sufficiently large, i.e., $T_i(s) = 1$. This case, indeed, corresponds to the harmonic frequencies far below $1/T_i$, i.e., $\omega_h << 1/T_i$, where $1/T_i$ is the bandwidth of the current measurement filter. In this case, $Z_{odq,WT}(s)$ from Eq. (8) is obtained as:

$$Z_{odq,WT}(s) = R_{f1} + L_{f1}s + PI(s). \tag{10}$$

From Eq. (9), the WT equivalent harmonic impedance at the kth harmonic $Z_{o,WT}(jk\omega_0)$ is obtained as:

$$Z_{o,WT}(jk\omega_0) = (R_{f1} + k_p) + j\left(L_{f1}h\omega_0 - \frac{k_i}{h\omega_0}\right),$$

$$\begin{cases} h = k-1 & \text{for positve sequence harmonic} \\ h = k+1 & \text{for negative sequence harmonic} \end{cases} \tag{11}$$

According to Eq. (11) and by neglecting the impact of the integrator gain k_i, the WT Norton equivalent model and WT equivalent harmonic impedance are approximately obtained as depicted in Figure 10.

Considering Figure 10, it is clear that in Case B, the real part of the output impedance is $k_p + R_{f1}$ and thus, the PI controller adds positive damping in the WT output impedance. This means that the PI controller adds positive damping for harmonics frequencies far below $1/T_i$, i.e., $\omega_h << 1/T_i$.

Case C: In this case, the bandwidths of the current and grid voltage measurements filters $T_i(s)$ and $T_v(s)$ with respect to harmonic frequencies are relatively low and thus, we set $T_i(s) \cong T_v(s) \cong 0$ for computing the WT output impedance at harmonic frequencies. According to Eq. (8) and by setting $T_i(s) \cong T_v(s) \cong 0$, we have:

$$Z_{odq,WT}(s) = R_{f1} + L_{f1}s + jL_{f1}\omega_0. \tag{12}$$

From Eq. (9), the WT equivalent harmonic impedance at the kth harmonic is obtained as:

$$Z_{o,WT}(jk\omega_0) = R_{f1} + jL_{f1}k\omega_0. \tag{13}$$

According to Eq. (13), the WT Norton equivalent model and WT equivalent harmonic impedance are obtained, as depicted in Figure 11.

It is clear that Case C corresponds to the simplified model in which the effect of the GSC control

$$Z_{o,WT}(jk\omega_0) = \begin{cases} Z_{odq,WT}\left(j(k-1)\omega_0\right) & \text{Positve sequence component} \\ {Z_{odq,WT}}^{*}\left(-j(k+1)\omega_0\right) & \text{Negative sequence component} \end{cases} \tag{9}$$

Box I

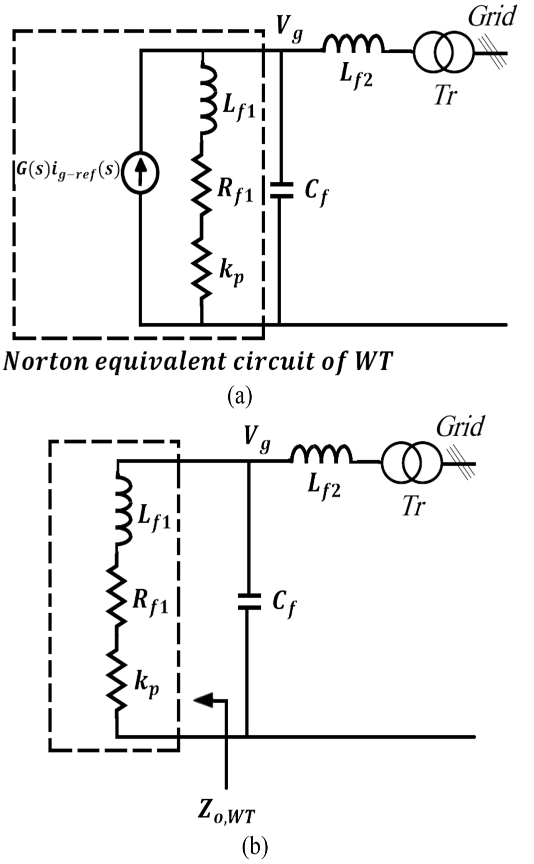

(a)

(b)

Figure 10. (a) Norton equivalent circuit of the WT system in Case B, (b) Equivalent harmonic impedance of the WT system in Case B.

on resonance frequencies is ignored, and each WT for resonance studies is modeled with the corresponding LCL filter interfaced between the GSC and grid. In Case C, the GSC current PI-controller does not add any damping action because this case is valid for harmonic frequencies far above the bandwidths of the current and voltage measurement filters, i.e., $\omega_h >> 1/T_i$ and $\omega_h >> 1/T_v$.

Case D: In this case, the dynamics of the current and voltage measurement filters are taken into account for computing WT equivalent harmonic impedance $Z_{o,WT}(jk\omega_0)$. Hence, $Z_{odq,WT}(s)$ and $Z_{o,WT}(jk\omega_0)$ are obtained using Eqs. (8) and (9).

6. HRMA and FS results of the study WPP with the model of Case C

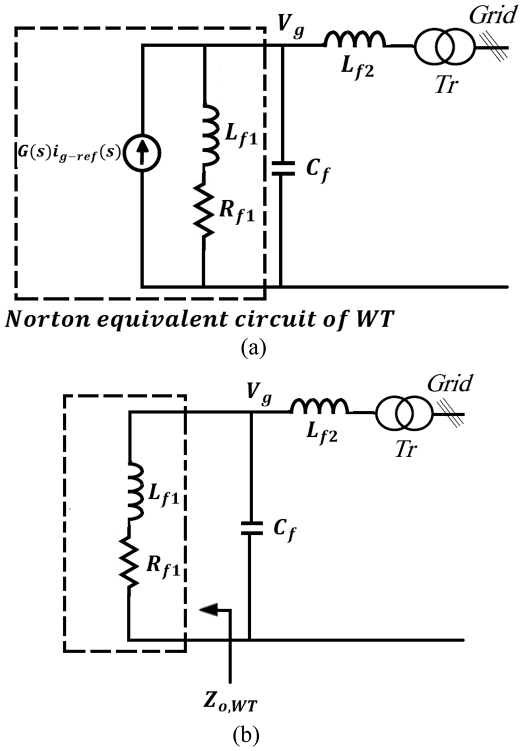

(a)

(b)

Figure 11. (a) Norton equivalent circuit of the WT system in Case C, (b) Equivalent harmonic impedance of the WT system in Case C.

Figure 12 depicts a simple model of the WPP of Figure 3 corresponding to Case C and it is used for harmonic resonance analysis. Figure 12 indeed corresponds to the simple model of Case C presented in Section 5, in which the effect of GSC control on resonance frequencies is ignored and each WT for resonance studies is modeled with the corresponding LCL filter interfaced between the GSC and grid. In Figure 12, there are 17 buses and each aggregated WT together with its back-to-back converter is considered as an ideal voltage source at harmonic frequencies. It is noted that an ideal voltage source is considered as short circuit in type in the resonance analysis; thus, in Figure 12, the GSCs are modeled as short circuit.

HRMA of the simple model in Figure 12 is performed in this section to find modal impedances and corresponding frequencies. In this way, the matrix $[Y_h(jh\omega)]$ at different harmonic frequencies is obtained and then, critical modes and corresponding modal impedances and frequencies as well as the buses having the highest contribution in the critical modes are obtained. Modal impedances can be determined by the inverse of each eigenvalue of the matrix $[Y_h(jh\omega)]$, i.e., $Z_{mi} = 1/\lambda_i$. The critical modes correspond to the modes in which the absolute values of corresponding eigenvalues reach the lowest values or the modes with the highest modal impedances. Hence, the resonance frequencies correspond to the frequencies with the highest values of modal impedances.

Table 1 shows the results of HRMA analysis corresponding to critical modes for the simplified model of the study system in Figure 12. Also, Figure 13 shows the absolute values of critical eigenvalues related to different resonance frequencies for the study system of Figure 12. The resonance frequencies in Figure 12 cor-

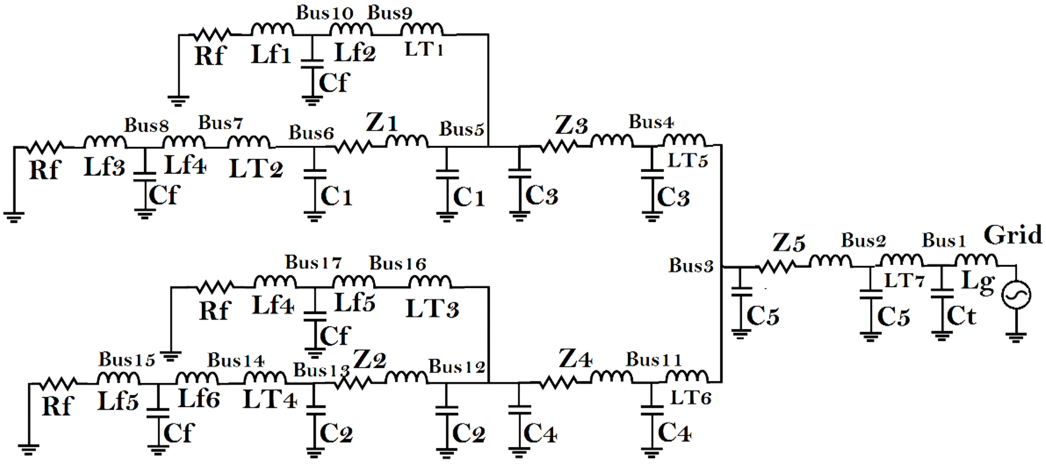

Figure 12. Impedance model of the system under study corresponding to Case C.

Table 1. Results of HRMA for the simple model of Case C in Figure 12.

Harmonic order (harmonic frequency in pu)	28.379	18.226	8.282	18.182	11.923	12.561	8.4	18.171
Mode number	6	17	6	13	16	7	10	14
Modal impedance Z_m (kΩ)	803.44	726.42	707.75	688.27	550.08	440.38	406.27	379.11
Dominant buses with highest participation factors	2,3,4,11	7,8,9,10, 14,15,16,17	All buses contribute in this mode	7,8,9,10, 14,15,16,17	7,8,14,15	7,8,14,15	All buses contribute in this mode	7,8,9,10, 14,15,16,17

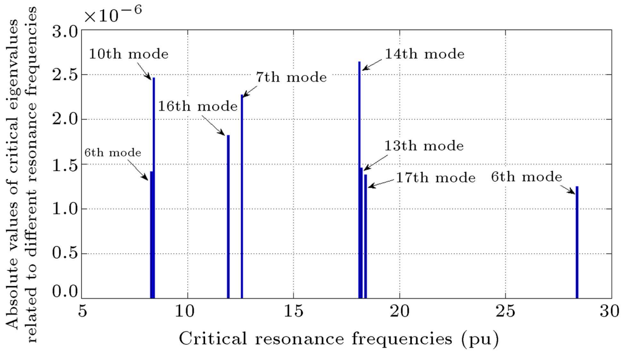

Figure 13. Absolute values of critical eigenvalues related to different resonance frequencies for the model of Case C in Figure 12.

respond to the frequencies with the lowest eigenvalues magnitudes.

The first row of Table 1 shows the resonance frequencies in per unit or the harmonic orders with large modal impedance. The second and third rows of Table 1 depict the mode number and corresponding modal impedance. In Table 1, the harmonic order, mode number, and modal impedance are arranged corresponding to criticality of the mode. The fourth row of Table 1 shows the buses having highest contribution in the critical modes and resonance frequencies. The buses with highest contribution in the resonance modes are extracted by calculating bus participation factors. The bus participation factors are obtained according to the explanations given in the last paragraph of Section 3.2.

According to the first column of Table 1 and Figure 13, the 6th mode at the harmonic order of 28.379 is the most critical mode, where the absolute value of the corresponding eigenvalue is 1.245×10^{-6} and the corresponding mode impedance is 803.44 kΩ. According to the fourth row of Table 1, buses 2, 3, 4, and 11 have made the most contribution in this mode.

It should be noted that some modes, like mode

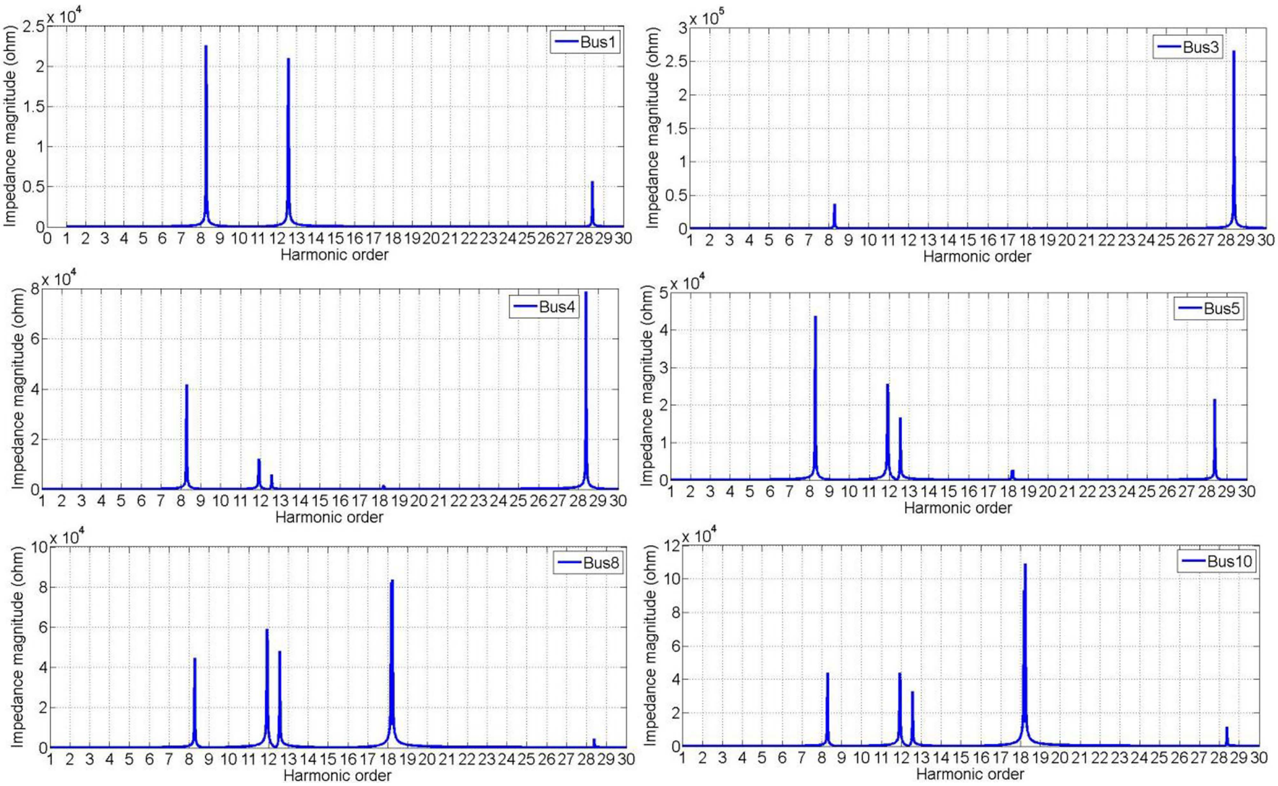

Figure 14. Frequency scan results at some buses of the system under study for the simplified model.

number 6, may have two resonant frequencies. As can be seen in Table 1, the critical resonant frequencies are around the 8th, 12th, 18th, and 28th orders.

According to Figure 14, there is a meaningful relationship between HRMA and FS results. According to Table 1, buses 1 and 3 have a negligible contribution in the resonance frequency orders of 18.171, 18.182, and 18.226. It is also observed in the FS plot of Figure 14 that buses 1 and 3 have zero driving point impedances in these harmonic orders. In the FS plot of Figure 14, buses 3 and 4 have the highest impedance magnitude at the harmonic order of 28.379. On the other hand, according to the HRMA analysis of Table 1, buses 2, 3, 4, and 11 have the highest participation factors in the critical mode with harmonic order of 28.379 and this outcome is in the agreement with the FS analysis results.

7. Simulation results and discussion

In Section 5, the WT output impedance was obtained for three simple cases (Cases A, B, and C) and one detailed case (Case D). In Cases A, B, and C, by neglecting the dynamics of the measurement filters, $T_i(s)$ and $T_v(s)$, and setting them equal to zero or 1, simplified expressions for the WT equivalent harmonic impedance $Z_{o,WT}$ were obtained. In this section, the FS and HRMA results related to different cases are given and compared; then, the effects of the bandwidths of the filters $T_i(s)$ and $T_v(s)$ and closed-loop bandwidth of the current control loop on harmonic resonance of the study WPP system are investigated.

It can be shown that the positive and negative sequence components of the WT output impedance at each harmonic are approximately identical; hence, for the harmonic resonance studies, we use the positive sequence component of the WT output impedance obtained from Eq. (9).

7.1. Comparison of HRMA and FS results for Cases A and C

Tables 1 and 2 show the results of HRMA analysis corresponding to critical modes for Cases C and A. The explanations regarding Table 1 were given in Section 6. In Table 1, the critical resonant frequencies are around the 8th, 12th, 18th, and 28th orders. Also, Figure 15

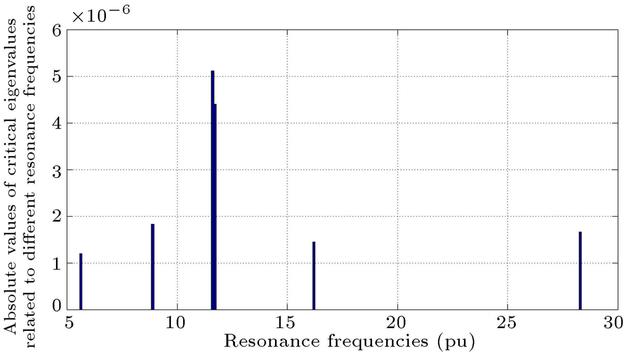

Figure 15. Absolute values of critical eigenvalues related to different resonance frequencies or the model of Case A.

Table 2. Results of HRMA for the model of Case A.

Harmonic order or harmonic frequency in pu	5.62	16.224	28.313	8.887	11.715	11.604
Mode number	11	13	6	16	11	12
Modal impedance Z_m (kΩ)	837.05	690.72	603.97	548.65	227.45	195.56
Dominant buses with highest participation factors	7,8,9,10,14 15,16,17	7,8,9,10,14, 15,16,17	2,3,4,11	7,8,14,15	1,7,8,14,15	1,7,8,14,15

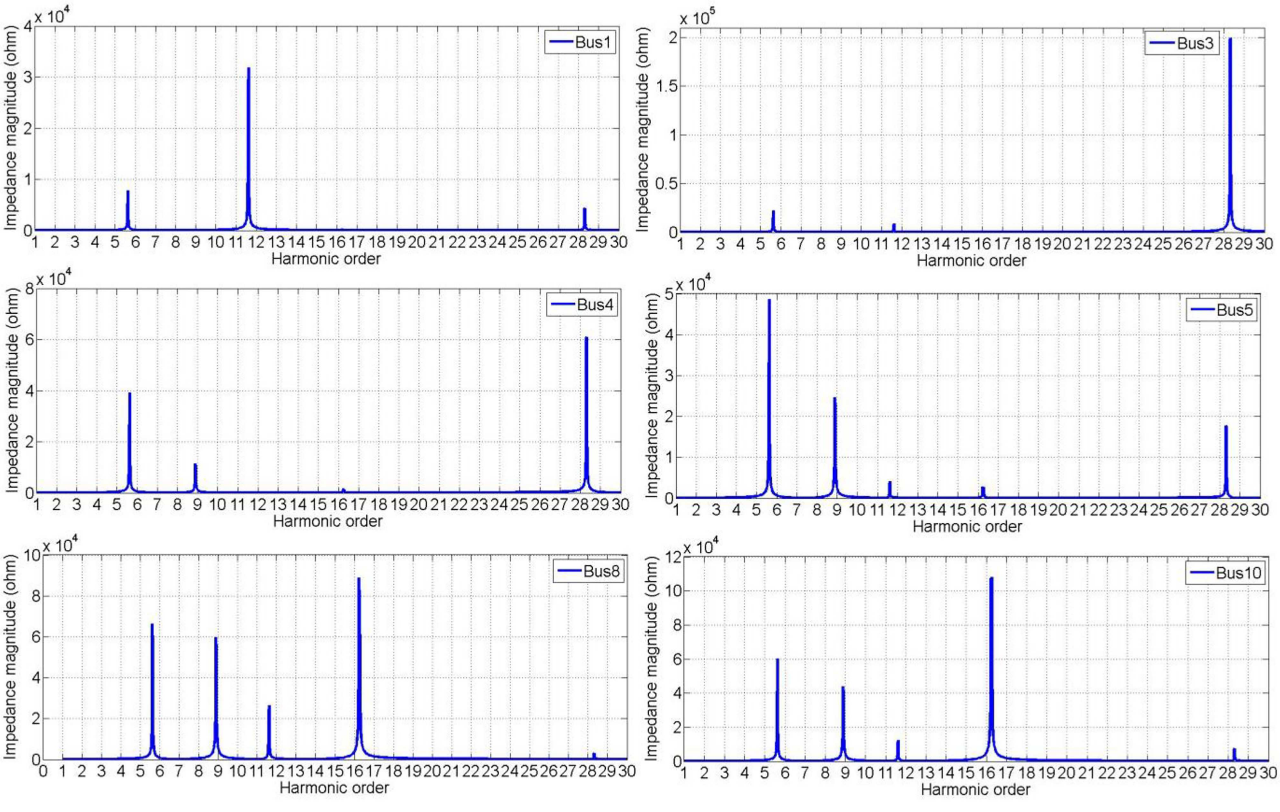

Figure 16. Frequency scan results at some buses of the system under study for Case A.

shows the absolute values of critical eigenvalues related to different resonance frequencies for the model of Case A. The resonance frequencies in Figure 15 are around the harmonic orders of 5.6, 8.88, 11.6, 11.7, 16.2, and 28.3 and correspond to the frequencies with the lowest eigenvalues magnitudes.

The participation factors show that the resonance frequencies around the 18th harmonic order are mostly related to the WPP buses, i.e., buses 8, 10, 15, and 17. According to Table 1, in Case C, the modal impedance for the harmonic order of 18.226 is 726.42 kΩ.

According to HRMA results of Table 2, in Case A, the resonance frequencies around the 5th and 16th orders are mostly related to the WPP buses, i.e., buses 8, 10, 15, and 17. According to Table 2, in Case A, the modal impedance values for the harmonic orders of 5.62 and 16.224 are 837.05 kΩ and 690.72 kΩ, respectively.

Also, Figure 16 shows the FS results related to

Case A for some buses of the study system. According to the FS results of Figure 16, buses 8 and 10 have the highest driving point impedances in the harmonic orders of 5.62 and 16.224.

According to HRMA results of Table 2, buses 2, 3, 4, and 11 have the highest contribution in harmonic order of 28.313 (1415.65 Hz). Therefore, in Figure 16, buses 3 and 4 have the highest driving point impedances in this harmonic order (1415.65 Hz). Comparison of Tables 1 and 2 shows that the WT harmonic output impedance model influences the resonance frequencies and the corresponding modal impedances of the entire grid. This means that by changing the WT harmonic impedance model, some resonance frequencies are shifted and new resonance frequencies such as 276 Hz (order 5.52) are created. According to Tables 1 and 2, bus 3 is the resonance center of harmonic order around 1400 Hz (order 28). Given that bus 3 has a significant distance from the buses connected to WPPs (i.e., buses 8, 10, 15, and 17), changing the WT harmonic impedance model cannot affect the resonance frequency of bus 3.

7.2. Comparison of HRMA and FS results for Cases B and C

Table 3 depicts the HRMA results of the study system once the WT output impedance model is considered as Case B (see, Figure 10(a) and (b)). Also, Figure 17 shows the modal impedance magnitudes at dominant resonance frequencies, obtained from the HRMA analysis for different cases. In this way, Figure 18 shows the critical eigenvalues with lowest magnitudes related to different resonance frequencies for the model of Case B. It is noted that the resonance frequencies correspond to the frequencies with the lowest eigenvalues magnitudes. Further, Figure 19 depicts the FS results of the study system related to Case B.

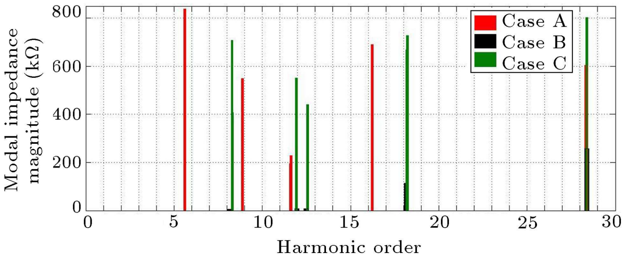

Figure 17. Modal impedance magnitudes at dominant resonance frequencies, obtained from the HRMA analysis.

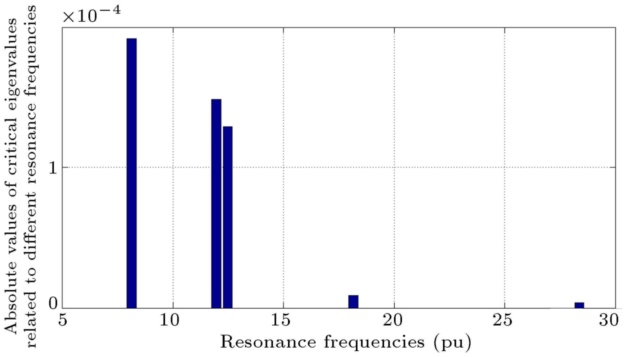

Figure 18. Absolute values of critical eigenvalues related to different resonance frequencies for the model of Case B.

Considering Table 3 and Figure 17, the critical resonant frequencies are around the 8th, 12th, 18th, and 28th orders. It is noted that the resonant frequencies and dominant buses participating in the resonance frequencies in Case B are approximately similar to the ones related to the Case C, given in Section 6. However, as shown in Figures 17 and 19 and Table 3, the magnitudes of modal impedances related to the Case B are significantly smaller than the ones related to Case C given in Table 1 and Figure 14. The results show that considering the WT output impedance model based on the model presented in Case B increases

Table 3. Results of HRMA for the model of Case B.

Harmonic order or harmonic frequency in pu	28.379	18.16	12.473	11.956	8.128
Mode number	6	17	12	17	11
Modal impedance Z_m (kΩ)	265.96	113.66	7.7555	6.726	5.2073
Dominant buses with highest participation factors	2,3,4,11	7,8,9,10,14 15,16,17	7,8,14,15	7,8,14,15	All buses contribute in this mode

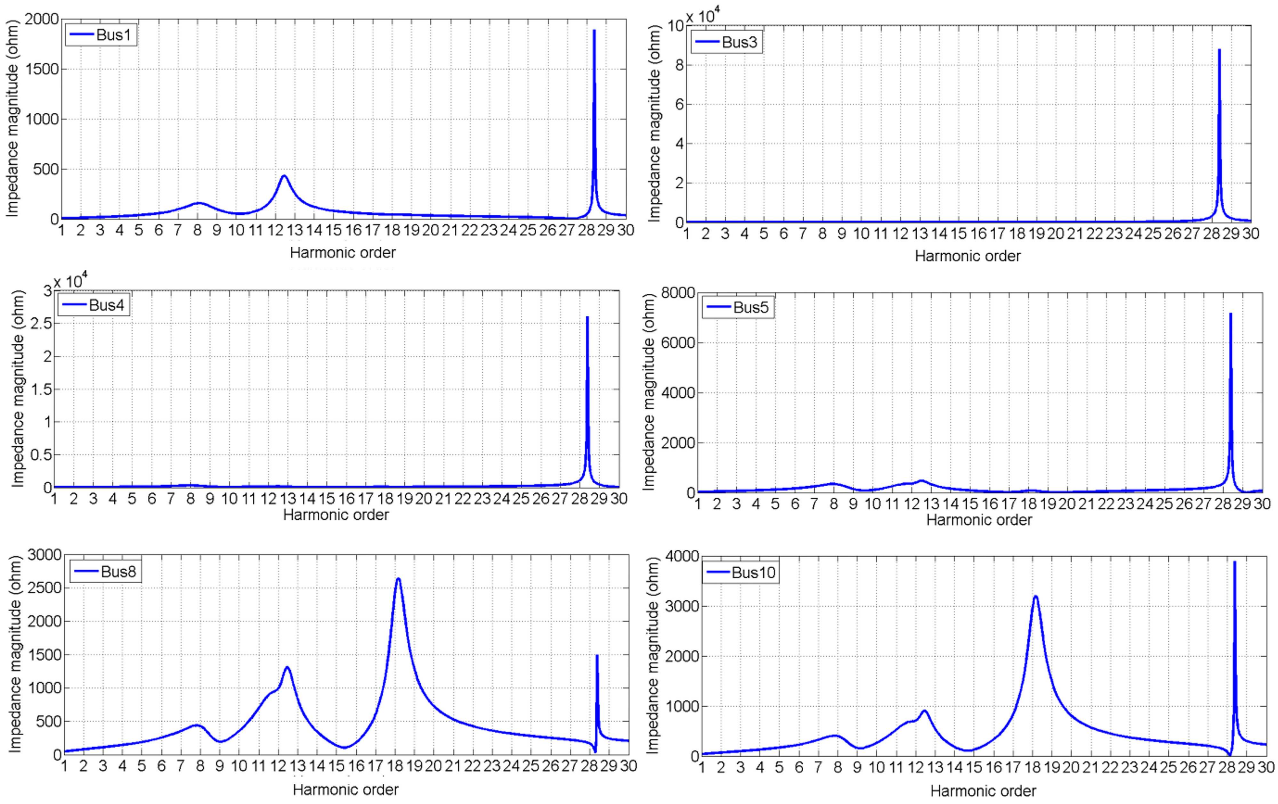

Figure 19. Frequency scan results at some buses of the system under study for Case B.

the damping of the resonance frequencies, but cannot shift the resonant frequencies. This is because the PI controller adds positive damping in the WT output impedance for harmonics frequencies far below $1/T_i$, i.e., $\omega_h << 1/T_i$.

7.3. Comparison of FS results for Cases A, B, C, and D

In this section, the impact of the WT harmonic impedance model on the FS result of the study system is studied. In Figure 20, the FS results of bus 8 related to Cases A, B, C, and D are given and compared. The bandwidths of the current and voltage measurement filters are considered as $\alpha_i = 1/T_i = 30$ pu $= 1500$ Hz and $\alpha_v = 1/T_v = 1$ pu $= 50$ Hz. Also, the GSC current control closed-loop bandwidth is set to $\omega_i = 4$ pu $= 200$ Hz, where the base of the grid frequency is $\omega_b = 2\pi \times 50$ rad/s.

According to Figure 20, the magnitudes of driving point impedances are close to each other in Cases B and D. Also, the resonance frequencies in the Cases B, C, and D are almost the same, but the resonance frequencies in Case A are very different from the other cases. In Cases B and D, the impact of the PI current controller related to the GSC is taken into account, and this consequently increases the resonance damping and, significantly, decreases the magnitudes of driving point impedances in the FS diagram.

7.4. Investigation of the effects of the bandwidths of the filters Ti(s) and Tv(s) on the FS results

In this section, the effects of the bandwidths of the current and voltage measurements filters on the FS results of bus 8 are discussed. In this study, the WT harmonic impedance model is considered as Case D and the GSC current control bandwidth is set to $\omega_i = 4$ pu $= 200$ Hz. Figures 21 and 22 depict six different FS plots of bus 8. In Figures 21(a), (b), and (c), the current filter bandwidth is considered as 750 Hz (15 pu) and three different values are considered for the voltage filter bandwidth, i.e., 50, 250, and 750 Hz (1 pu, 5 pu, and 15 pu).

Also, in Figures 22(a), (b), and (c), the current filter bandwidth is considered as 1500 Hz (30 pu), and similar to Figure 21, three different values (50, 250, and 750 Hz) are considered for the voltage filter bandwidth.

Comparison of six graphs shows that increasing the bandwidth of the voltage filter can propagate new resonant frequencies in the network. According to Figure 22(a), it is clear that at a sufficiently large value of current measurement filter bandwidth and a small voltage measurement filter bandwidth, the model of Case D can be approximated by the model of Case B. Also, from Figure 22(c), by increasing the voltage filter bandwidth, the output impedance model in Case D has a resonance behavior similar to that of the output

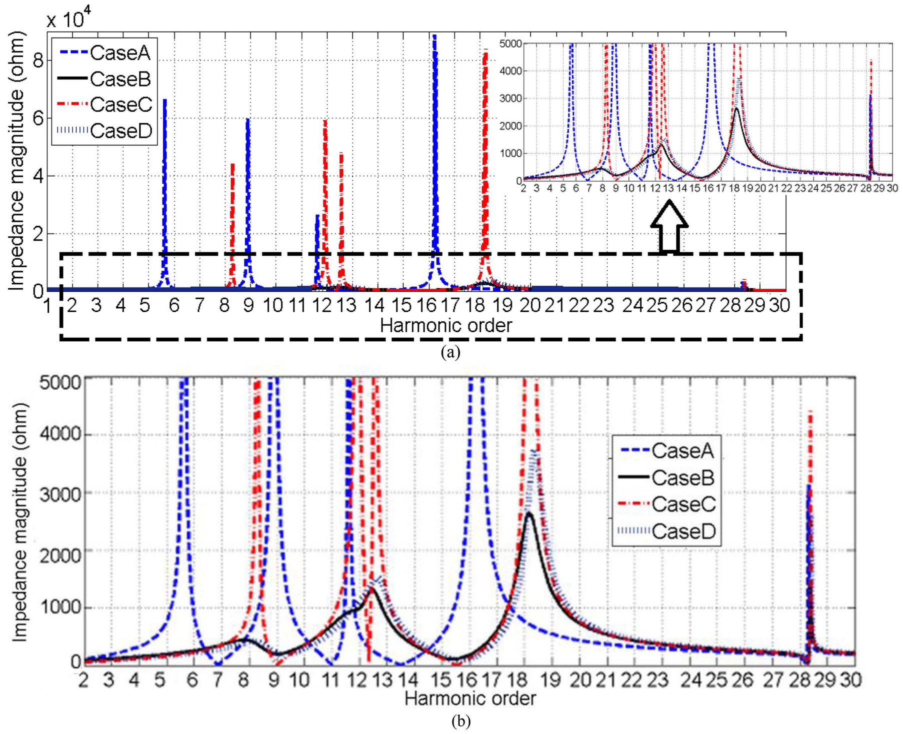

Figure 20. (a) Frequency scan results at bus 8 for Cases A, B, C and D, (b) Frequency scan results at bus 8 with higher resolution for better depiction of Cases B and D.

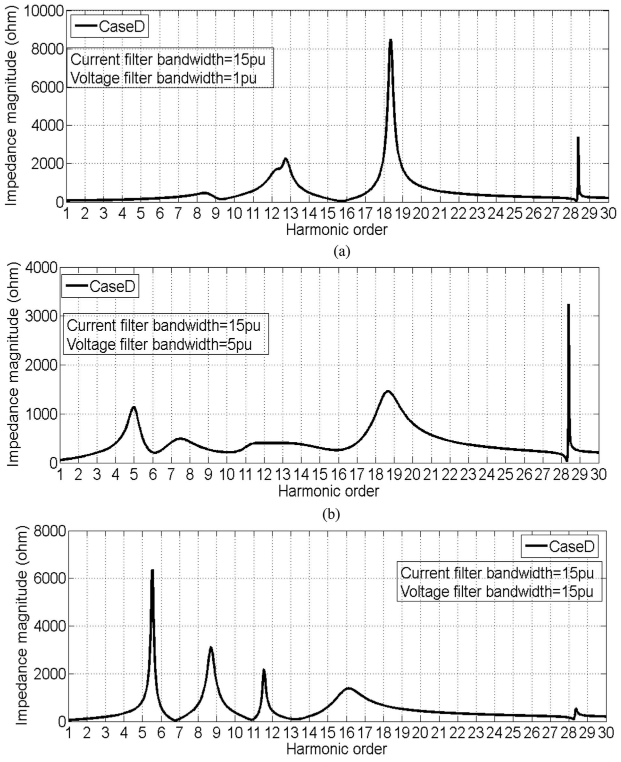

Figure 21. Effects of the bandwidth of the voltage measurement filter on the frequency scan results of bus 8 for the current measurements filter bandwidth of 750 Hz (15 pu), (a) voltage filter bandwidth set to 50 Hz (1 pu), (b) voltage filter bandwidth set to 250 Hz (5 pu), and (c) voltage filter bandwidth set to 750 Hz (15 pu).

impedance model mentioned in Case A. However, the magnitudes of the driving point impedances in Case D are much lower than the ones in Case A.

7.5. Investigation of the effects of the GSC current control bandwidth on the FS results

Figure 23 shows the effects of the GSC current control bandwidth on the FS results of bus 8. In Figure 23, the WT harmonic output impedance model is based on the Case D, the bandwidths of the current and voltage measurements filters are set to 1500 Hz and 50 Hz (30 pu and 1 pu), respectively, and different values are considered for the GSC current control bandwiths (i.e., 50, 150, and 750 Hz or 1, 3, and 5 pu).

As shown in Figure 23(a), resonant frequencies in Case D and in the current control bandwidth of 50 Hz (or 1 pu) are similar to the ones in Case C. However, the magnitudes of the driving point impedances in Case D are much lower than the ones in Case C.

Therefore, once the GSC current control bandwidth is low, the WT harmonic impedance model based on the Case C can be an appropriate approximation to show resonance frequencies in the network. According to Figures 23(b) and (c), increasing the bandwidth of the current control loop cannot shift the resonant frequencies, but it enhances the system damping and, consequently, reduces the driving point impedances in the resonance frequencies.

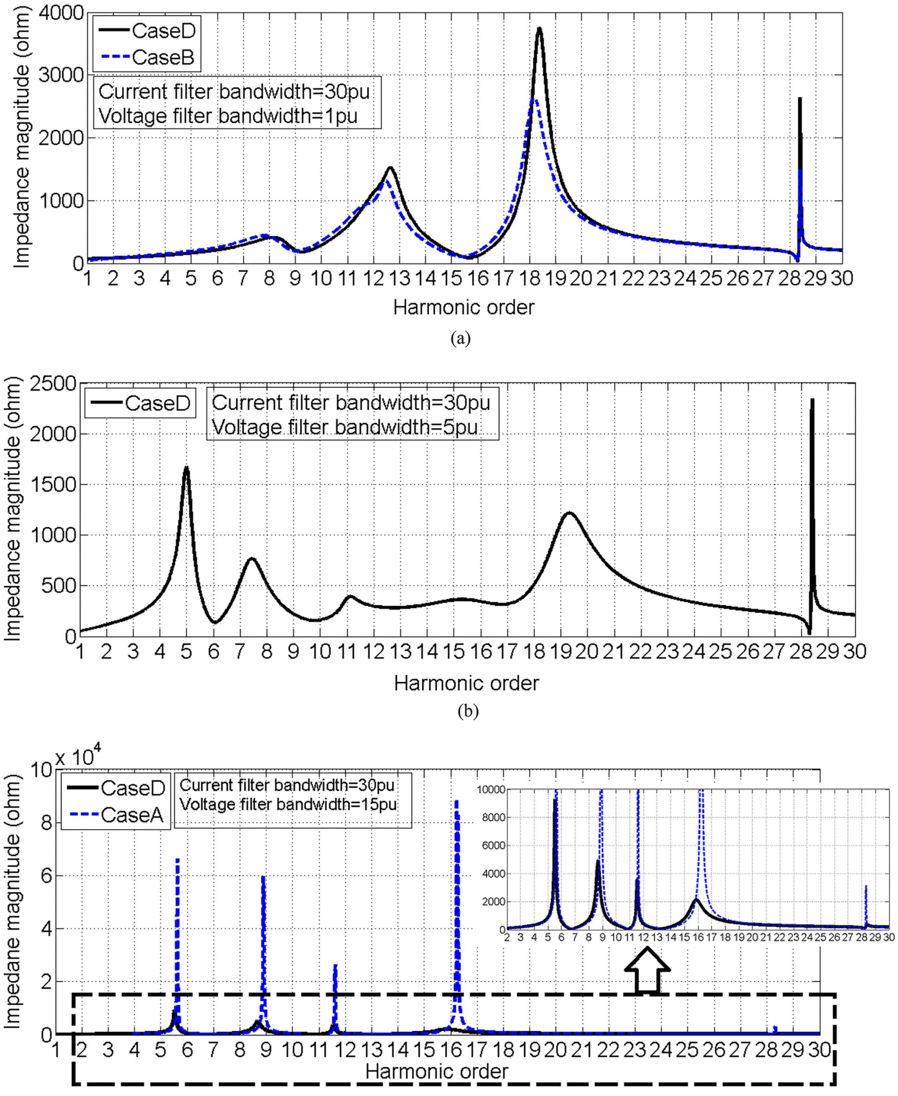

(a)

(b)

(c)

Figure 22. Effects of the bandwidth of the voltage measurement filter on the frequency scan results of bus 8 for the current measurements filter bandwidth of 1500 Hz (30 pu), (a) voltage filter bandwidth set to 50 Hz (1 pu), (b) voltage filter bandwidth set to 250 Hz (5 pu), and (c) voltage filter bandwidth set to 750 Hz (15 pu).

7.6. Time domain simulation results

In variable speed WTs, the 5th, 7th, 11th, and 13th harmonics are the dominant ones with highest magnitudes. In this section, four sets of passive filters are used for damping of harmonic resonances and for mitigation of 5th and 7th harmonics and harmonic orders higher than 11. Each passive filter set comprises two second-order tuned passive filters for mitigation of the 5th and 7th harmonics and one second-order high-pass filter for mitigation of the 11th and higher-order harmonics.

Figure 24 shows the Norton equivalent model of the study system in Case C with and without passive filters. In Figure 24, buses 8, 10, 15, and 17 are considered as current injection buses and thus, harmonic currents at the orders of 5, 7, and 11 together with the fundamental current are injected into these buses. Figure 25 shows time responses and frequency spectrum and THD of currents at the branch (1–2) of Figure 24 for the cases with and without passive filters. According to Figure 25, by using passive filters, harmonic currents in different branches have been weakened and the THD has been considerably decreased.

8. Conclusion

The system under study in this paper was a 400 MW Wind Power Plant (WPP) comprising PMSG-based Wind Turbines (WTs) connected to a 150 kV grid through interfaced LCL filters, cables, and power transformers. This study investigated the harmonic

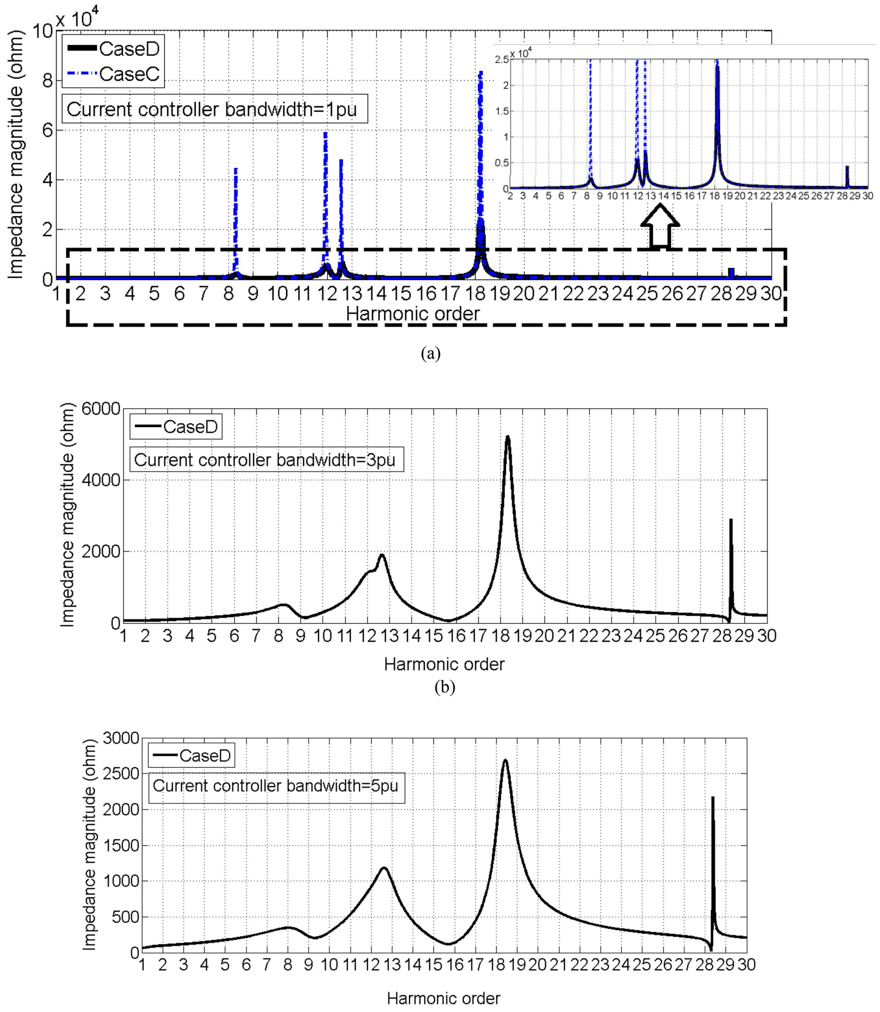

(a)

(b)

(c)

Figure 23. Effects of the GSC current control bandwidth on the bus scan results of bus 8, (a) on the bus ω_i $\omega_i = 5$ pu = 250 Hz, (b) $\omega_i = 1$ pu = 50 Hz, and (c) $\omega_i = 3$ pu = 150 Hz.

resonance analysis of the study WPP system by taking the impacts of the Grid-Side Converter (GSC) control and current and voltage measurement filters into account. In this way, the WT harmonic impedance models of the WTs were presented for three simple cases (Cases A, B, and C) and one detailed case (Case D). Then, WT harmonic impedance was calculated for the mentioned cases. Next, the frequency scan and Harmonic Resonance Mode Analysis (HRMA) results related to different cases were given and compared, and then effects of the bandwidths of the current and voltage measurements filters and closed-loop bandwidth of the WT current control loop on harmonic resonance analysis of the study WPP system were presented.

According to the obtained results, the following statements are given:

- Resonant frequencies in Case D and for the current control bandwidth of 50 Hz (or 1 pu) were similar to the ones in Case C. However, the magnitudes of the driving point impedances in Case D were much lower than the ones in Case C. Therefore, once the GSC current control bandwidth is low, the WT harmonic impedance model based on the Case C can be an appropriate approximation to show resonance frequencies in the network;
- According to the results, increasing the bandwidth of the current control loop could not shift the resonant frequencies, but enhanced the system damping and, consequently, reduced the driving point impedances in the resonance frequencies;
- It was shown that at a sufficiently large value of current measurement filter bandwidth and a small value of voltage measurement filter bandwidth, the model of Case D could be approximated by the model of Case B if the GSC current control bandwidth was selected around the 4 pu;
- The resonance frequencies in the Cases B, C, and D

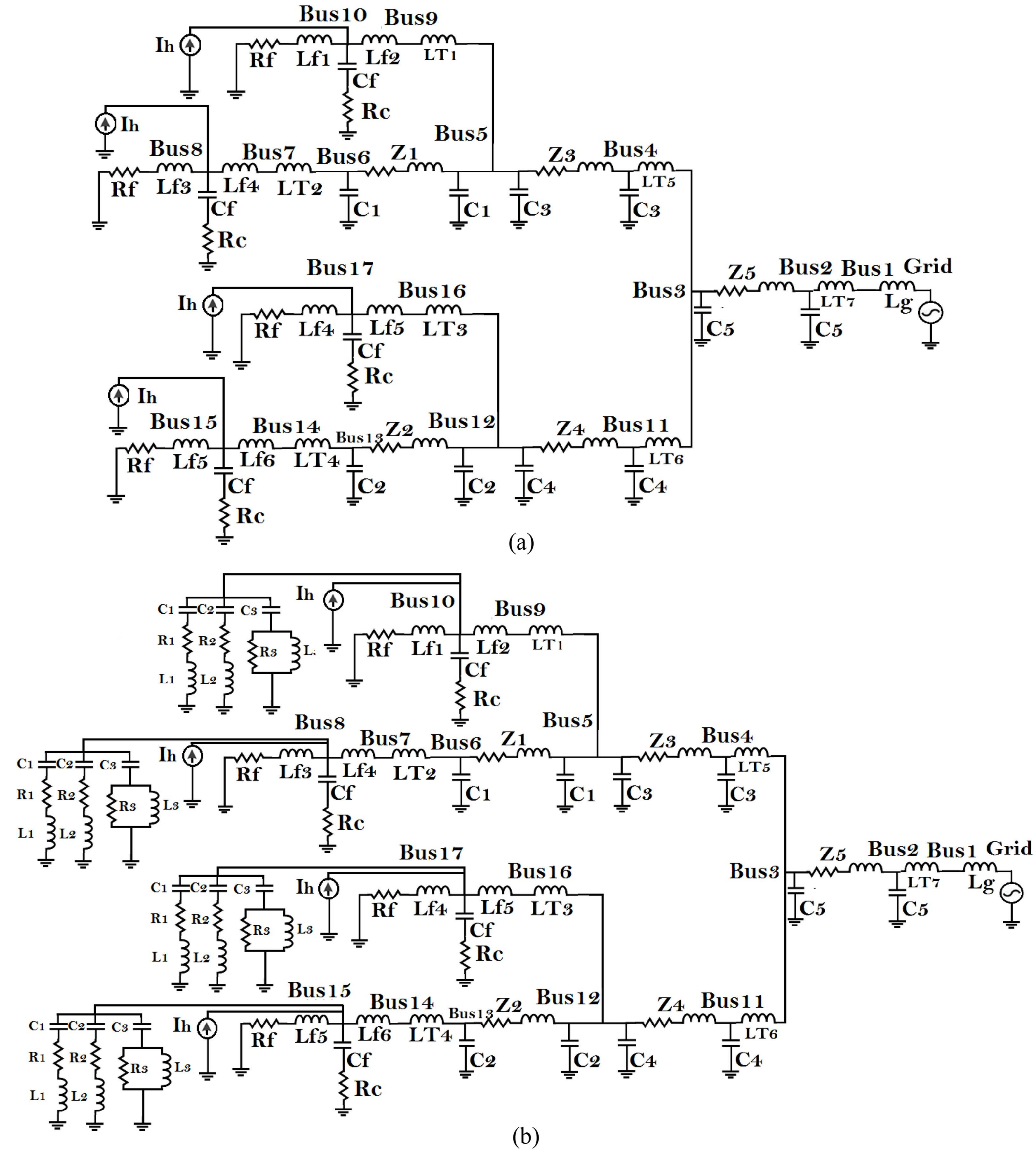

(a)

(b)

Figure 24. Norton equivalent model of the study system in Case C: (a) without passive filters and (b) with placing passive filters at buses 8, 10, 15, and 17.

were almost the same, but the resonance frequencies in Case A were very different from those in the other cases. In Cases B and D, the impact of the PI current controller related to the GSC was taken into account, and this consequently increased the resonance damping and significantly decreased the magnitudes of driving point impedances in the frequency scan diagram;

- By increasing the voltage filter bandwidth to a greater extent, the output impedance model in Case D exhibited a resonance behavior similar to that of the output impedance model mentioned in Case A. However, the magnitudes of the driving point impedances in Case D were much lower than the ones in Case A.

Nomenclature

WPP	Wind Power Plant
PMSG	Permanent Magnet Synchronous Generator
WT	Wind Turbine
VSWTs	Variable Speed Wind Turbines
VSC	Voltage Source Converters
f_{res}	Resonance frequency
X_{eq}	Equivalent circuit reactance
f_h	Frequency
$[V_h]$	Vector of nodal harmonic voltages
$[Z_h]$	Harmonic impedance matrix
$[I_h]$	Vector of injected harmonic currents

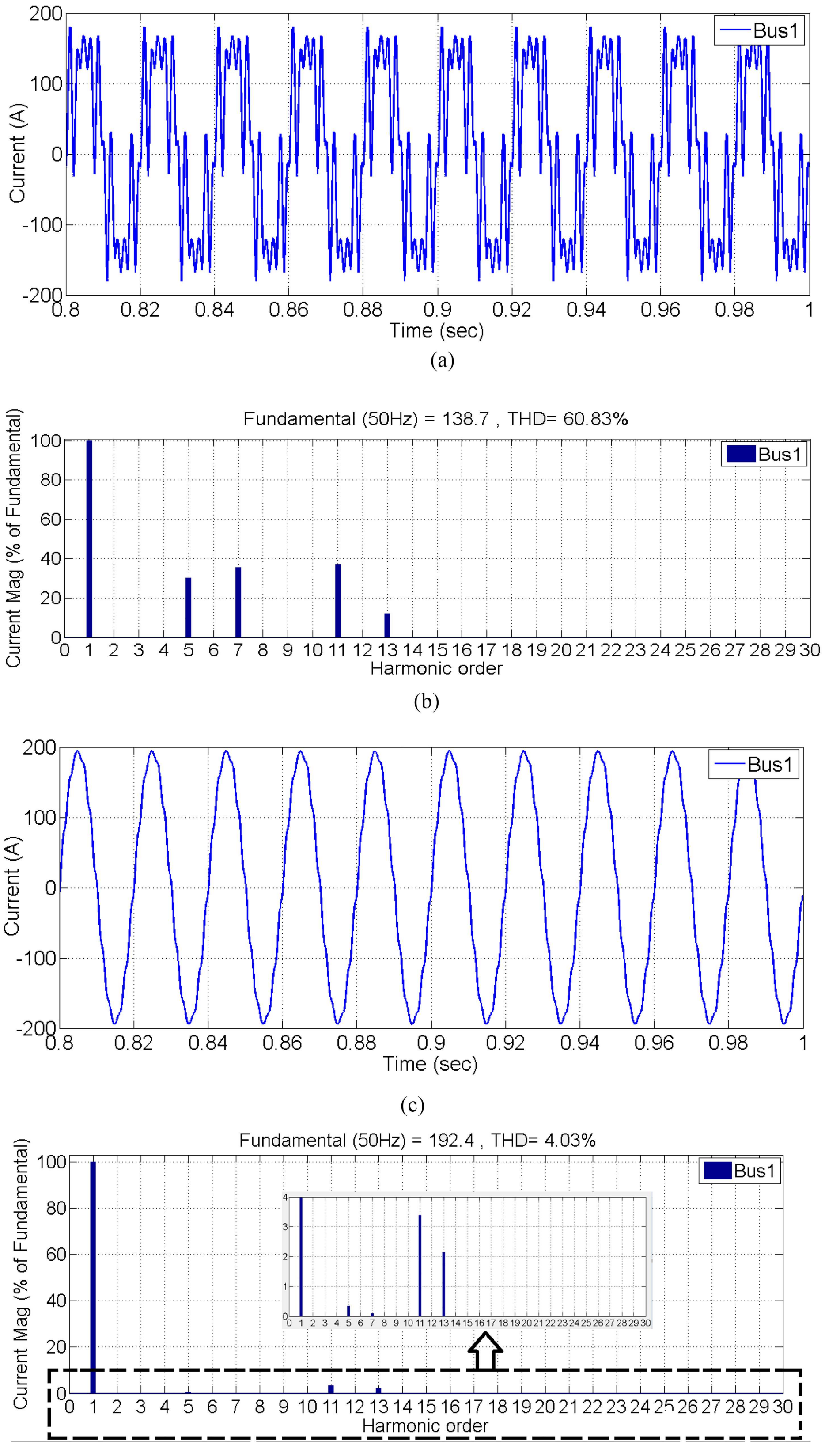

(a)

(b)

(c)

(d)

Figure 25. Time responses and frequency spectrum of current at branch (1-2), (a) current without passive filter, (b) frequency spectrum without passive filter, (c) current with passive filter, and (d) frequency spectrum with passive filter.

$[\psi_h]$	Left eigenvector matrices
$[\Phi_h]$	Right eigenvector matrices
$[\Lambda_h]$	Diagonal eigenvalue matrix
$[V_m]$	Modal voltage vector
FS	Frequency scan
HRMA	Harmonic Resonance Mode Analysis
DFIG	Doubly Fed Induction Generator
GSC	Grid-Side Converter
$[Y_h]$	Network admittance matrix
$\hat{v_{gdq}}$	Filtered converter grid voltage
ω_i	Closed loop bandwidth of the GSC control loop
$Z_{o,WT}(s)$	Output impedance
$\hat{i_{gdq}}$	Filtered converter current
$[I_m]$	Modal current vector

References

1. Jahanpour-Dehkordi, M., Vaez-Zadeh, S., and Mohammadi, J. "Development of a combined control system to improve the performance of a PMSG-based wind energy conversion system under normal and grid fault conditions", *IEEE Trans. Energy Conversion*, **34**(3), pp. 1287–1295 (2019).

2. Liu, H., Xie, X., He, J., et al. "Sub synchronous interaction between direct-drive PMSG based wind farms and weak AC networks", *IEEE Trans. Power Systems*, **32**(6), pp. 4708–4720 (2017).

3. Du, W., Dong, W., and Wang, H.F. "Small-signal stability limit of a grid-connected PMSG wind farm dominated by the dynamics of PLLs", *IEEE Trans. Power Systems*, **35**(3), pp. 2093–2107 (2020).

4. He, J., Huang, L., Wu, D., et al. "Frequency support from PMSG-based wind turbines with reduced DC-link voltage fluctuations", *CES Trans. Electrical Machines and Systems*, **2**(3), pp. 296–302 (2018).

5. Das, S. and Subudhi, B. "A H∞ robust active and reactive power control scheme for a PMSG-based wind energy conversion system", *IEEE Trans. Energy Conversion*, **33**(3), pp. 980–990 (2018).

6. Rahimi, M. "Modeling, control and stability analysis of grid connected PMSG based wind turbine assisted with diode rectifier and boost converter", *Electrical Power and Energy Systems-Elsevier,* **93**, pp. 84–96 (2017).

7. Kocewiak, L., Bak, L., and Hjerrild, J. "Harmonic aspects of offshore wind farms", *PhD Seminar on Detailed Modelling and Validation of Electrical Components and Systems*, Fredericia, Denmark (2010).

8. Bradt, M., Badrzadeh, B., Camm, E., et al. "Harmonics and resonance issues in wind power plants", *IEEE Power and Energy Society- Wind Plant Collector System Design Working Group* (2010).

9. Nisak, K., Candela, I., Rauma, K., et al. "An overview of harmonic analysis and resonances of a large wind power plant", *Annual Conf. IEEE Industrial Electronics Society,* (7–10 November 2011).

10. Kocewiak, L.H., *Harmonics in Large Offshore Wind Farms*, Ph.D. Dissertation, Dept. Energy Tech., Aalborg Univ., Aalborg, Denmark (2012).

11. Bollen, M.H.J. and Yang, K. "Harmonic aspects of wind power integration", *J. Modern Power Syst. Clean Energy,* **1**(1), pp. 14–21 (Jun. 2013).

12. Badrzadeh, B. and Gupta, M. "Power system harmonic analysis in wind power plants-Part II: Practical experiences and mitigation methods", In *Conf. Rec. IEEE IAS Annu. Meeting,* pp. 1–8 (2012).

13. Zheng, R. and Bollen, M.H.J. "Harmonic resonances associated with wind farms", *Dept. Eng. Sci. and Math., Lulea Univ. of Tech.*, Lulea, Sweden,Tech. Rep. (Jul. 2010).

14. Wakileh, G.J., *Power System Harmonics-Fundamentals, Analysis and Filter Design*, Springer (2001).

15. Li, J., Samaan, N., and Williams, S. "Modeling of large wind farm systems for dynamic and harmonics analysis", *Transmission and Distribution Conference and Exposition*, T&D, IEEE/PES, pp. 1–7 (2008).

16. Bradt, M., Badrzadeh, B., Camm, E., et al. "Harmonics and resonance issues in wind power plants", In *Proc. IEEE PES Gen. Meet.*, pp. 1–8 (2011).

17. Caixia, Y., Kaipei, L., and Dongxu, W. "Harmonic resonance circuit's modeling and simulation", *Power and Energy Engineering Conference*, pp. 1–5 (2009).

18. Lay, D.C. "Linear algebra and its applications", ISBN: 0321314859, Boston:Pearson/Addison-Wesley (2006).

19. Esmaili, M., Ali Shayanfar, H., and Jalilian, A. "Modal analysis of power systems to mitigate harmonic resonance considering load models", *Energy,* **33**, pp. 1361–1368 (2008).

20. Binti, K.N., Rauma, K., Luna, A., et al. "Harmonic compensation analysis in offshore wind power plants using hybrid filters", *IEEE Trans. Industry Applications*, **50**(3), pp. 2050–2060 (2014).

21. Ruma, K. "Electrical resonances and harmonics in a wind power plant", MSc. Thesis, Dept. Energy Tech., Aalborg Univ., Aalborg, Denmark (2012).

22. Kocewiak, L.H., Kramer, B.L.O., Holmstrom, O., et al. "Resonance damping in array cable systems by wind turbine active filtering in large offshore wind power plants", *IET Renew. Power Gener*, **11**(7), pp. 1069–1077 (2017).

23. Md. Hasan, K.N.B., Rauma, K., Luna, A., et al. "Harmonic compensation analysis in offshore wind power plants using hybrid filters", *IEEE Trans. Ind. Applications*, **50**(3), pp. 2050–2060 (2014).

24. Liu, H. and Sun, J. "Voltage stability and control of offshore wind farms with AC collection and HVDC transmission", *IEEE Journal of Emerging and Selected Topics in Power Electronics*, **2**(4), pp. 1181–1189 (2014).

25. Vargas, U. and Ramirez, A. "Extended harmonic domain model of a wind turbine generator for harmonic transient analysis", *IEEE Trans. Power Delivery*, **31**(3), pp. 1360–1368 (2016).

26. Buchhagen, C., Rauscher, C., Menze, A., et al. "First experiences with harmonic interactions in converter dominated grids", *International ETG Congress*, pp. 1–7 (2015).

27. Chen, X. and Sun, J. "A study of renewable energy systems harmonic resonance based on a DG test-bed", *26th IEEE Applied Power Electronics Conference and Exposition*, pp. 995–1002 (2011).

28. Harnefors, L., Bongiorno, M., and Lundberg, S. "Input-admittance calculation and shaping for controlled voltage source converters", *IEEE Trans. Ind. Elec.*, **54**, pp. 3323–3334 (2007).

29. Cespedes, M. and Sun, J. "Modeling and mitigation of harmonic resonance between wind turbines and the grid", *Proc. IEEE Energy Conversion Congress and Exposition*, pp. 2109–2116 (2011).

30. Cespedes, M. and Sun, J. "Impedance modeling and analysis of grid-connected voltage-source converters", *IEEE Trans. Power Electronics*, **29**(3), pp. 1254–1261 (2014).

31. Wang, X., Blaabjerg, F., and Wu, W. "Modeling and analysis of harmonic stability in an AC power-electronics-based power system", *IEEE Trans. Power Electronics,* **29**, pp. 6421–6432 (2014).

32. Bayo-Salas, A., Beertenyz, J., Rimez, J., et al. "Impedance-based stability assessment of parallel VSC HVDC grid connections", *11th IET Int. Conf. on AC and DC Power Transmission,* pp. 1–9 (Feb. 2015).

33. Liu, Z., Rong, J., Zhao, G., and Luo, Y. "Harmonic assessment for wind parks based on sensitivity analysis", *IEEE Trans Sustainable Energy*, **8**(4), pp. 1373–1382 (2017).

34. Axelsson, U., Holm, U., Bollen, M., et al. "Propagation of harmonic emission from the turbines through the collection grid to the public grid", *Proc. 22nd Int. Conf. and Exhibition on Electricity Distribution (CIRED 2013)*, pp. 1–4 (2013).

35. Zheng, R., Bollen, M., and Zhong, J. "Harmonic resonances due to a grid-connected wind farm", *14th Int. Conf. Harmonics and Quality of Power*, pp. 1–7 (Sept. 2010).

36. Sainz, L., Monjo, L., Pedra, J., et al. "Effect of wind turbine converter control on wind power plant harmonic response and resonances", *IET Electric Power Applications*, **11**(2), pp. 157–168 (2016).

37. Ebrahimzadeh, E., Blaabjerg, F., Wang, X., et al. "Reducing harmonic instability and resonance problems in PMSG based wind farms", *IEEE Journal of Emerging and Selected Topics in Power Electronics*, **6**(1), pp. 73–83 (2018).

38. Zhang, S., Jiang, S., Lu, X., et al. "Resonance issues and damping techniques for grid-connected inverters with long transmission cable", *IEEE Trans. Power Elec.*, **29**(1), pp. 110–120 (2014).

39. Lukasz, H.K., Hjerrild, J., and Bak, C.L. "Harmonic models of a back-to-back converter in large offshore wind farms compared with measurement data", *Nordic Power Conference*, Denmark (2009).

40. Patel, D., Varma, R.K., Seethapathy, R., et al. "Impact of wind turbine generators on network resonance and harmonic distortion", *Canadian Conf. on Electrical and Computer Engineering (CCECE)* (May, 2010).

41. Sankaran, C., *Power Quality*, Boca Raton, FL: CRC Press (2002).

42. Chang, C., Chan, S., and Teng, J. "A fast method for driving point impedance calculation of unbalanced distribution system", *IEEE International Conference on Systems & Signals (ICSS 2005)*, pp. 134–138 (2005).

43. Lukasz, H.K., Hjerrild, J., and Bak, C.L. "Wind farm structures impact on harmonic emission and grid interaction", *European Wind Energy Conference*, Poland (2010).

44. Esmaili, M., Shayanfar, H.A., and Jalilian, A. "Modal analysis of power system to mitigate harmonic resonance considering load models", *Energy*, **33**, pp. 1361–1368 (2008).

45. Nisak, K., Candela, I., Rauma, K., et al. "An overview of harmonic analysis and resonances of a large wind power plant", *Annual Conf. IEEE Ind. Elec. Society* (2011).

46. Beiki, A. and Rahimi, M. "An efficient sensorless approach for energy conversion enhancement and damping response improvement in permanent magnet synchronous generator (PMSG) based wind turbines", *Int Trans Electr Energ Syst.*, **29**(1), pp. 1–18 (2019).

Appendix A

Parameters of the aggregated wind power plant are given below in Table A.1.

Table A.1. System parameters.

Component	The name of the component	Electrical value
Grid reactor	L_g	19.3 mH
The capacitance of the tuned filter	C_t	5.658 μF
Converter transformer	LT7	19.33 mH
Transmission cable	Z_5	
- Series resistance		0.056 Ω
- Series inductance		1.0 mH
- Shunt capacitance		0.52 μF
Inter farm cables	Z_1, Z_2, Z_3, Z_4	
- Series resistance		0.372 Ω
- Series inductance		18.181 mH
- Shunt capacitance		0.05709 μF
Generator transformer	LT1, LT2, LT3, LT4	0.04346 H
LCL filter		
- Wind turbine side	Lf1, Lf3, Lf5, Lf7	0.2109 H
- Capacitor	C_f	0.70736 μF
- Grid side	Lf2, Lf4, Lf6, Lf8	0.00214 H
-Rf		1.3254 Ω
High voltage transformer	LT5, LT6	38.674 mH

Biographies

Ashkan Beiki received his BSc degree in Electrical Engineering in 2010 from Shiraz University of Technology (SUT), Shiraz, Iran. He obtained the MSc degree in Electrical Power Engineering from University of Isfahan, Isfahan, Iran in 2013. He obtained his PhD degree in Electrical Engineering from University of Kashan, Kashan, Iran in 2019. Currently, he is with Mana Energy Pak Company. His current research interests include renewable energy sources and wind turbines.

Mohsen Rahimi received his BSc degree in Electrical Engineering in 2001 from Isfahan University of Technology, Isfahan, Iran. He obtained both his MSc and PhD degrees in Electrical Engineering from Sharif University of Technology (SUT), Tehran, Iran in 2003 and 2011, respectively. He joined the Department of Electrical and Computer Engineering at University of Kashan, Kashan, Iran as an Assistant Professor in 2011. Currently, he is an Associate Professor at University of Kashan, and his major research interests include modeling and control of renewable energy sources, wind turbines, and microgrids.